

# EES Batteries

Accepted Manuscript

This article can be cited before page numbers have been issued, to do this please use: S. Biswas, T. Köhler, A. Mohammad, H. Stöcker and D. C. Mayer, *EES Batteries*, 2025, DOI: 10.1039/D5EB00054H.



This is an Accepted Manuscript, which has been through the Royal Society of Chemistry peer review process and has been accepted for publication.

Accepted Manuscripts are published online shortly after acceptance, before technical editing, formatting and proof reading. Using this free service, authors can make their results available to the community, in citable form, before we publish the edited article. We will replace this Accepted Manuscript with the edited and formatted Advance Article as soon as it is available.

You can find more information about Accepted Manuscripts in the [Information for Authors](#).

Please note that technical editing may introduce minor changes to the text and/or graphics, which may alter content. The journal's standard [Terms & Conditions](#) and the [Ethical guidelines](#) still apply. In no event shall the Royal Society of Chemistry be held responsible for any errors or omissions in this Accepted Manuscript or any consequences arising from the use of any information it contains.

# Composite Cathode Material for Improved Aluminum-Polymer Batteries<sup>†</sup>

Shuvrodev Biswas,<sup>\*a</sup> Thomas Köhler,<sup>a</sup> Amir Mohammad,<sup>a</sup> Hartmut Stöcker,<sup>a</sup> and Dirk C. Meyer,<sup>ab</sup>

<sup>a</sup> Institute of Experimental Physics, TU Bergakademie Freiberg, Leipziger Str. 23, 09599 Freiberg, Germany. Tel: +4973 3646; E-mail: shuvrodev.biswas@physik.tu-freiberg.de <sup>b</sup> Center for Efficient High-Temperature Material Conversion, TU Bergakademie Freiberg, Winkler Str. 5, 09599 Freiberg, Germany.

## Broader context

Rechargeable aluminum batteries have gained significant research interest due to their high theoretical capacity, safety, and material abundance. However, their widespread application is hindered by challenges such as cathode degradation, poor conductivity, and limited cycle life, primarily caused by the corrosive nature of electrolytes. Addressing these issues, a composite cathode material combining phenanthrenequinone (PQ) and graphite is proposed, which exhibits twice the conductivity and improved stability in solid polymer electrolytes. Our study reveals that PQ and graphite actively participate in the electrochemical process through two distinct mechanisms: the intercalation of  $\text{AlCl}_4^-$  into graphite and the coordination reaction between PQ and  $\text{AlCl}_2^+$ . This collaborative interaction results in enhanced capacity, cyclability, and energy density, making aluminum polymer batteries an interesting option for next-generation batteries. Furthermore, the composite performs consistently across different graphite types, highlighting its adaptability. These advancements contribute to the broader goal of sustainable energy storage, offering a safer, more abundant, and cost-effective alternative to conventional battery technologies for future applications.



Cite this: DOI: 00.0000/xxxxxxxxxx

Composite Cathode Material for Improved Aluminum-Polymer Batteries<sup>†</sup>Shuvrodev Biswas,<sup>\*a</sup> Thomas Köhler,<sup>a</sup> Amir Mohammad,<sup>a</sup> Hartmut Stöcker,<sup>a</sup> and Dirk C. Meyer,<sup>ab</sup>Received Date  
Accepted Date

DOI: 00.0000/xxxxxxxxxx

Rechargeable aluminum batteries (RABs) are an emerging post-lithium technology for their large ore reserves and better safety properties. However, conventional cathode materials like graphite have limited storage capacity because the intercalation of  $\text{AlCl}_4^-$  occurs only in every third or fourth layer of graphite. On the other hand, organic compounds with a different working principle lack stability in the strongly Lewis acidic electrolytes due to rapid dissolution. Hence, this investigation presents a composite consisting of an organic compound 9,10-phenanthrenequinone (PQ) and graphite as a cathode material for improved RABs. For the melt diffusion synthesis, spherical graphite (SPG) was used at a ratio of 2:3 to PQ. A recently developed solid polymer based on aluminum chloride ( $\text{AlCl}_3$ ), triethylamine hydrochloride ( $\text{Et}_3\text{NHCl}$ ) and polyamide (PA6) was used as electrolyte. The combination of fabricated composite and solid polymer electrolyte (SPE) with an Al anode offered significant improvement in capacity and cyclability compared to pure SPG or pure PQ cathodes. The cyclic voltammetry analysis showed that both components contribute to the capacity, which was also confirmed by *operando* XRD, FT-IR, XPS, and EPR analysis. Therefore, both intercalation and coordination reactions take place synergetically. Additionally, SPG was exchanged with meso carbon micro-beads (MCMC) and graphite flakes (GF), which demonstrated no considerable impact of the graphite particle shape on the cathode performance.

## 1 Introduction

In today's world, lithium-ion batteries (LiBs) are dominating the sector of rechargeable batteries due to their tremendous progress in performance. However, there are still some issues like safety concerns<sup>1</sup>, high costs of raw materials, i.e. lithium and cobalt,<sup>2</sup> and challenges like co-intercalation and the poor oxidative stability of conventional electrolytes<sup>3</sup> so that researchers are looking for alternative chemistries beyond LiBs. Among all the potential replacements for LiBs, rechargeable aluminum batteries (RABs) have drawn immense attention for their availability (3rd most abundant element on earth), impressive theoretical volumetric ( $8056 \text{ mA h cm}^{-3}$ ), and gravimetric ( $2981 \text{ mA h g}^{-1}$ ) capacities considering a three-electrons process<sup>4</sup>, and comparatively safer chemistry<sup>5</sup>. Despite the exceptional properties exhibited by Al-metal anodes, the performance of rechargeable aluminum batteries (RABs) remains inadequate for practical commercial deployment.

One of the primary challenges is the fabrication of suitable cathodes that have sound compatibility with electrolytes<sup>6</sup> and facilitate multivalent Al ion storage. In particular, intercalating the trivalent  $\text{Al}^{3+}$  ion into crystalline host structures poses inherent challenges attributable to the strong coulombic attractions within the anionic frameworks because of high activation energies<sup>7,8</sup>. The high activation energy promotes rapid complexation of  $\text{Al}^{3+}$  with ions like  $\text{Cl}^-$ , which inhibits its direct intercalation into the host structure. Therefore, instead of the preliminary assertion of having three electrons from a single Al atom, the most studied cathode graphite offers only 3 electrons from 8 Al atoms by the insertion of  $\text{AlCl}_4^-$ <sup>9,10</sup>:



In the search for cathode materials with a higher number of transferred electrons, so far, only a few cathodes (e.g.  $\text{V}_2\text{O}_5$  nanowires,  $\text{TiO}_2$  nanotube arrays,  $\text{MoS}_2$  microspheres, etc.) have been reported to intercalate  $\text{Al}^{3+}$  ions<sup>11–13</sup>. However, apart from the early-mentioned strong coulombic attractions, these materials also suffer from low electrical conductivity, lack of suitable electrolyte match, unwanted side reactions, rapid capacity fading, and limited cyclability<sup>14–16</sup>. In addition to the cathodes with intercalation mechanism, coordination reaction-based cathode ma-

<sup>a</sup> Institute of Experimental Physics, TU Bergakademie Freiberg, Leipziger Str. 23, 09599 Freiberg, Germany; E-mail: shuvrodev.biswas@physik.tu-freiberg.de

<sup>b</sup> Center for Efficient High-Temperature Material Conversion, TU Bergakademie Freiberg, Winkler Str. 5, 09599 Freiberg, Germany.

<sup>†</sup> Electronic supplementary information (ESI) available. See DOI: 00.0000/00000000.



terials, specifically organic materials like polycyclic aromatic hydrocarbons (PAH), conductive polymers, and tetradiketones are explored by several research groups because of their structural diversity and flexibility, sufficient intermolecular spaces to ease the strain management and storage of complex Al carrier ions, e.g.  $\text{AlCl}_2^{2+}$  and  $\text{AlCl}_2^+$ .<sup>17,18</sup> For instance, Anthraquinone<sup>19</sup>, 9,10-phenanthrenequinone<sup>20</sup>, Tetradiketone<sup>21</sup>, and their derivatives have exhibited promising performance. Nonetheless, they are inhibited by rapid dissolution and low electrical conductivity, leading to poor cyclability and significant capacity loss. To resolve these challenges, a composite of 9,10-phenanthrenequinone and activated carbon<sup>22</sup>, poly(phenanthrenequinone) (pPQ)<sup>23</sup>, polythiophene (PT)<sup>24</sup>, a macrocycle of phenanthrenequinone or a hybrid of pPQ and graphite flakes (PQ- $\Delta$ -HY)<sup>20</sup> are potential research directions. Still issues like poor electrical conductivity, low nominal voltage, and the use of highly corrosive ionic liquid (IL) electrolytes persist.

In ionic liquid (IL) electrolytes, such as  $\text{AlCl}_3\cdot\text{Et}_3\text{NHCl}$ <sup>25</sup>,  $\text{AlCl}_3\cdot\text{pyridinium chloride}$ <sup>26</sup>,  $\text{AlCl}_3\cdot\text{urea}$ <sup>27</sup>,  $\text{AlCl}_3\cdot 1\text{-ethyl-3-methylimidazolium chloride}$  ([EMIM]Cl)<sup>28,29</sup>,  $\text{AlCl}_3\text{-NaCl-KCl}$ <sup>30</sup>,  $\text{AlCl}_3\text{-NaCl-LiCl-KCl}$ <sup>31</sup> the electrochemically active species  $\text{Al}_2\text{Cl}_7^-$  acts as a source of anolytes for the electrochemical deposition of aluminum<sup>25,32</sup>, which is crucial for battery functioning. However, these electrolytes possess certain disadvantages, especially their extremely corrosive nature and susceptibility to moisture, impacting both Coulombic efficiency and cycling stability<sup>33</sup>. As a result, these limitations curtail the commercialization of aluminum batteries in large-scale energy storage. Addressing these issues, IL-based polymer electrolytes were introduced, which can lower moisture sensitivity, and electrolyte leakage and also enable separator-free RABs<sup>34-37</sup>. In one of our recent studies, we presented an iono-polymer electrolyte based on polyamide (PA6)<sup>38</sup> with some promising results, however, the capacity with spherical graphite cathodes is still compromised.

Herein, addressing all the above points, this study presents a composite cathode material based on PQ and SPG synthesized by a one-step melt diffusion process for RABs using an  $\text{Et}_3\text{NHCl}:\text{AlCl}_3$ -based solid polymer electrolyte (see Figure S1, ESI<sup>†</sup>). The iono-polymer electrolyte is flexible, easy to prepare, and suitable for commercial cell housings because of reduced leakage and corrosivity<sup>38</sup>. With this approach, the capacity ( $C_{\text{cathode}}$ ) can be increased with a higher nominal voltage, i.e. better energy density compared to the individual components. Moreover, we propose a combination of coordination and intercalation ion transfer mechanisms supported by *operando* X-ray diffraction (XRD), fourier transform infrared spectroscopy (FT-IR), X-ray photoelectron spectroscopy (XPS), electron spin resonance spectroscopy (ESR) and cyclic voltammetry (CV). Considering the variation in electrochemical performance associated with the morphology of different graphite forms<sup>39</sup>, we investigate their role as host materials for PQ in RABs. Additionally, the effect of temperature on the performance of RABs using SPE is explored.

## 2 Results and discussion

### 2.1 Properties of the composites

The composite formed a mold like the shape of the container after heat treatment (see Figure S1 a, ESI<sup>†</sup>), which was the first indication of a successful fabrication through melt diffusion, because melted PQ worked as a binder for the graphite particles. To study the changes in surface morphology, concentric backscattered electron microscopy (CBS) analysis was done using a FEI Helios Nanolab 600i with an acceleration voltage of 10 kV and a current of 69 nA. The study shows that the composite shown in Figure 1 d had no shape like its components (Figure 1 a and 1 b). Although the milling process could potentially influence this disparity, Figure 1 c suggests otherwise. The ball milling does not appear to significantly alter the particle shapes, as evidenced in Figure 1 c. However, a slight deformation of the SPG particles is noticeable, particularly in the inset of Figure 1 c. Hence, the considerable explanation is that the PQ particles completely melt and adhere to the surface of the deformed graphite particles during the melt diffusion process. As a result, the composite particles exhibit smooth surfaces, in contrast to the layered structure of the graphite particles (compare Figure 1 b and 1 d with inset). Such smooth surfaces of the particles confirm a well-synthesized composite, which is also claimed by Yoo et al. for their composite of activated carbon and PQ<sup>22</sup>.

To determine the quantity of PQ present in the SPGPQ composite material, a thermogravimetric analysis (TGA) was conducted under argon atmosphere using a Setaram TGDSC + IR 120523. The samples (4.5 mg of each) were heated from room temperature to 600 °C at a heating rate of 10 K/min. Figure 1 e shows the TGA analysis of an SPGPQ composite sample and the two starting materials (pure PQ and SPG powder). It can be seen that the pure PQ powder is completely vaporized at around 260 °C (melting temperature 206 °C). In comparison, there is no change in the pure SPG powder. On the other hand, the composite material shows a weight loss of around 57 % at approximately 270 °C. From this, it can be concluded that the PQ has completely evaporated and the composite consists of approx. 43 wt.% graphite (close to a 3:2 ratio).

The powder diffraction patterns of the composite are also different from the diffraction patterns of PQ and SPG. Figure 1 f, shows that diffractions of PQ either disappeared or shifted after the formation of the composite due to the reduction of crystallinity. The reflections that could be attributed to PQ, such as those at  $2\theta = 12^\circ$ ,  $14^\circ$ ,  $20^\circ$ , and  $24^\circ$ , were also significantly suppressed in intensity. Similar trends are also observed at higher angles. Such reduced crystallinity is also reported for PQ composites with activated carbon<sup>22</sup>. The intensity of graphite 002 reflection in the composite was also significantly decreased compared to pure graphite. This characteristic can be attributed to the coating of the PQ onto the graphite particles or the partial reduction of graphite to graphene oxides due to annealing at 250 °C<sup>40,41</sup>. The position ( $26.4^\circ$ ) and width of the reflection is almost similar to the reflection of pristine SPG, implying that SPG particles were functioning well as hosts for the PQ melts.

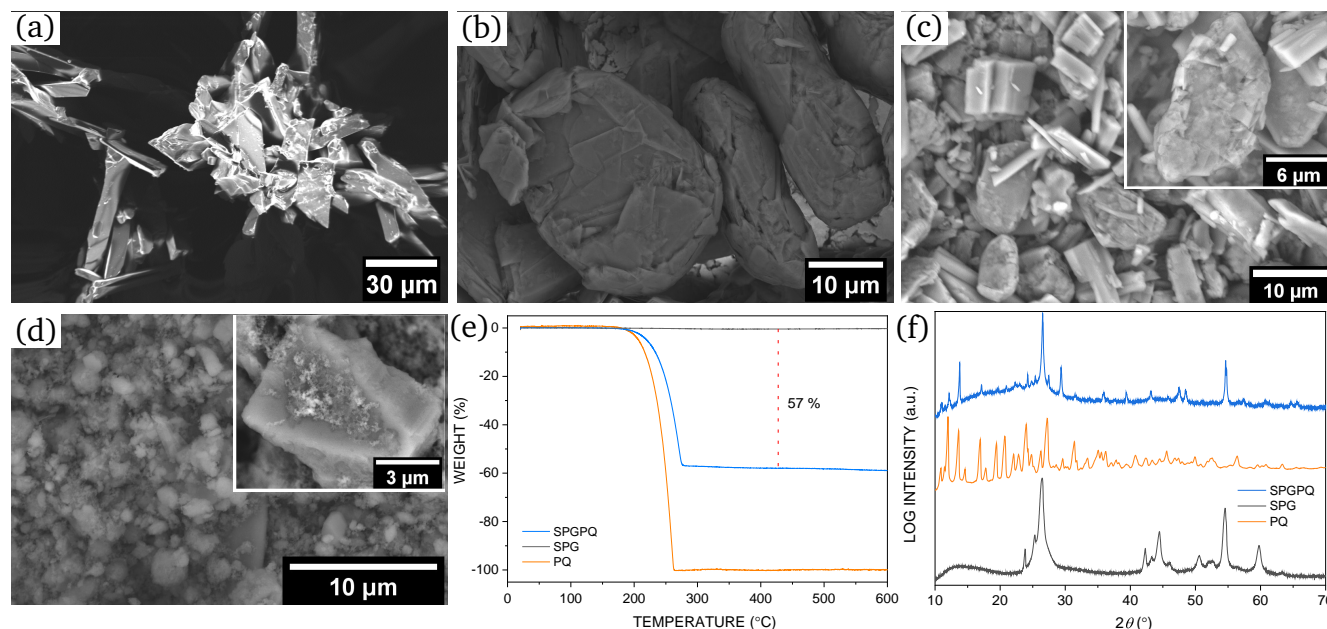


**Fig. 1** Comparison between properties of SPGPQ and its components: CBS images of a) PQ, b) SPG, c) SPGPQ composite (after 30 min of milling), inset: slightly deformed particles, d) SPGPQ composite (after melt diffusion), inset: smooth surface of one particle indicating the composite formation, e) TGA analysis, and f) XRD of all materials.

## 2.2 Stability of the composite in the electrolyte

The stability of the composite and its components in solid polymer electrolytes was investigated via attenuated total reflection (ATR) in the infrared range (FT-IR spectroscopy). PQ and SPGPQ electrodes were kept in contact with the electrolyte for 5 min and 30 min to analyze the caused changes. Figure 2 a and b show that the pure PQ electrode is unstable in the ionic polymer and reacts over time. The FT-IR spectra of the PQ without air contact show clear differences for 5 min and 30 min and longer time led to more pronounced changes in the IR spectra. Particularly, the change in the spectral range of the carbonyl stretching vibration ( $\nu$  C=O) shows a clear shift from  $1673\text{ cm}^{-1}$  to  $1542\text{ cm}^{-1}$ . This shift can be attributed to the complexation of  $\text{AlCl}_x$  species at the electroactive C=O group, forming a  $\text{C=O}-[\text{AlCl}_x]^{3-x}$  complex<sup>19,23,42</sup>.

In addition, broad and prominent vibrational modes are observed at  $762\text{ cm}^{-1}$  and  $483\text{ cm}^{-1}$ , whereby the former could have its origin in the bending vibration of the new carbonyl complex and the latter could be assigned to adsorbed electrolyte residues. The latter is plausible, as it is the typical vibrational range of species like  $\nu$   $\text{AlCl}_4^-$  and  $\nu$   $\text{Al}_2\text{Cl}_7^-$ <sup>38</sup>. The other vibrational modes, for example, the bending vibration  $\delta$  C–H–C and  $\delta$  C–C–C at  $1120\text{--}1163\text{ cm}^{-1}$  and  $1230\text{--}1333\text{ cm}^{-1}$  respectively, are reduced in intensity. It is seen that the  $\delta$  C-ring mode ( $763\text{ cm}^{-1}$ ) and  $\nu$  C=C ( $1450\text{ cm}^{-1}$ ) intensity are almost unchanged, which confirms the statement about complexation only in the carbonyl group. This observation indicates a purely chemical, rather than electrochemical, interaction with the electrolyte under an Ar atmosphere, which is unfavorable for stable battery performance.

Interestingly, the vibration modes exhibit recovery upon air contact, and within approximately 150 s the spectrum of the C=O

stretching vibrational mode is almost restored. In both cases, similar characteristics are observed. Such observation suggests that the complexation is limited to the surface and happens with a highly reactive and transient species, which interacts rapidly with air and then decomposes.

The behavior of the composite SPGPQ is quite stable (see Figure 2 c and d) with no significant spectral changes observed even after 30 min of contact with the electrolyte. The strong resemblance of these SPGPQ spectra to that of the pristine PQ cathode (shown in blue at the top of Figure 2 c and d), is a clear indication of a successful synthesis and the enhanced chemical stability against the strong Lewis acid. The  $\text{C=O}-[\text{AlCl}_x]^{3-x}$  complexation is also absent, so that there are no changes in the relevant PQ vibration modes, i.e. C=C and C=O, while the sample was exposed to air. This confirms that the composite avoids the undesirable chemical interaction seen in pure PQ, making it a more suitable cathode material for reversible electrochemical processes in batteries.

## 2.3 Ion transfer mechanism

### 2.3.1 Intercalation of $\text{AlCl}_4^-$ species

Figure 3 a shows the diffraction pattern of a cell with SPG cathode with a voltage-time plot during charging and discharging. The 5<sup>th</sup> cycle is considered for analyzing the data compared to the diffraction pattern of the as-prepared cell. It is clearly seen that the graphite 002 reflection is partly shifted with the increase of voltage while charging and at 2.35 V, when the cell is completely charged, there are 3 reflections at  $2\theta$  of  $20.7^\circ$ ,  $26.6^\circ$ , and  $27.8^\circ$  for the SPG cathode. The observed peak shifting and emergence of new peaks are in good agreement with the literature<sup>29,43</sup>. The persistent reflection at  $26.6^\circ$  may be attributed to inactive graphite material.



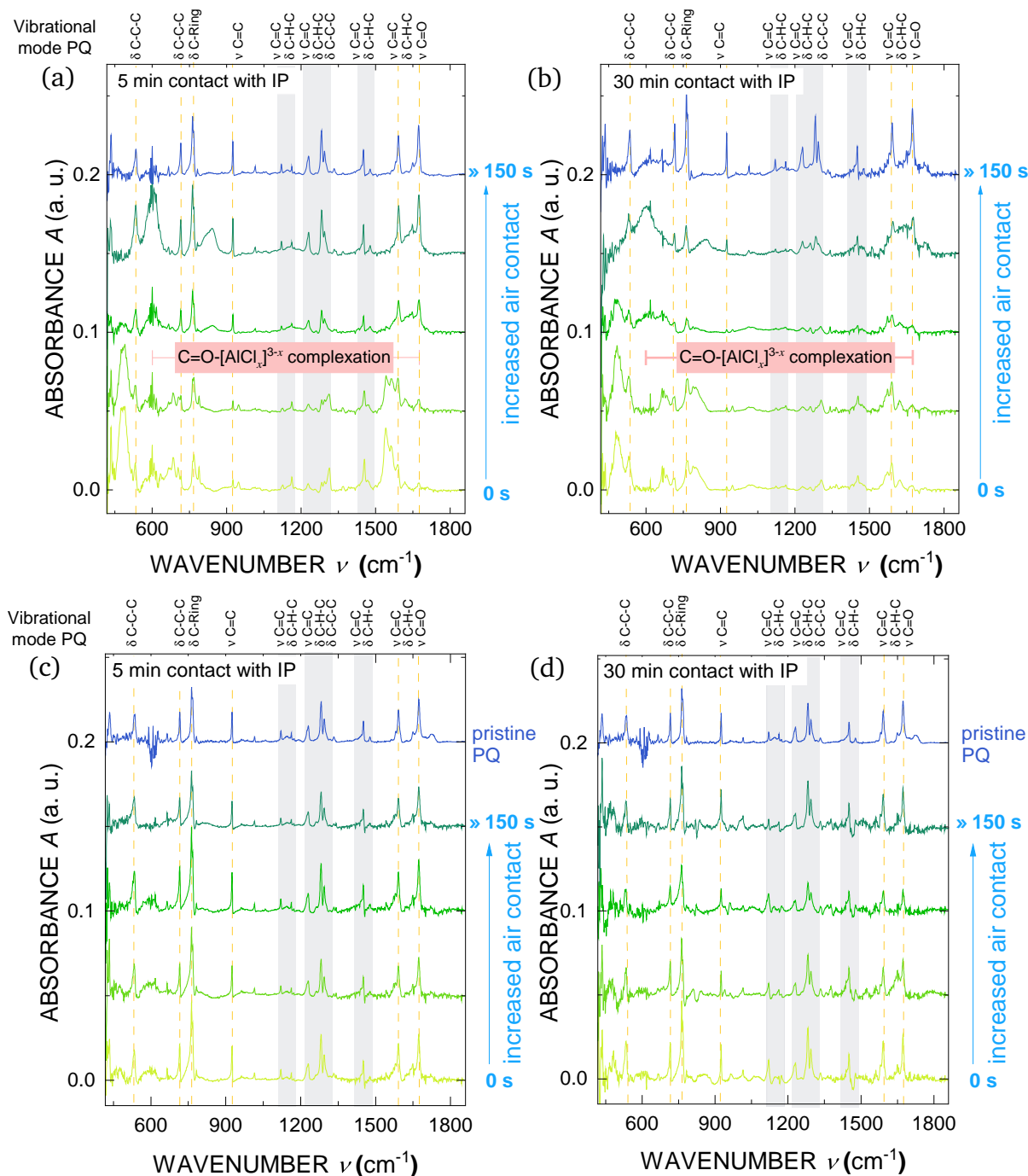


**Fig. 2** FT-IR spectra comparison showing the stability of electrodes in SPE: PQ electrodes after (a) 5 min and (b) 30 min of contact; SPGPQ composite electrodes after (c) 5 min and (d) 30 min of contact with the spectrum of the pristine PQ cathode shown at the top (blue). The vibration modes of pure PQ are indicated.

The XRD data suggest well-defined staging and long-range order in the anion-graphite intercalation structures, comparable to stage-4 intercalation of  $\text{AlCl}_4^-$  into graphite at room temperature, as suggested by Pan et al<sup>44</sup>. The reflections at  $20.7^\circ$  and  $27.6^\circ$  gradually emerge while charging, whereas the original reflection at  $26.6^\circ$  is losing some intensity. This development can be attributed to a structural evolution of graphite from stage  $n$  to stage  $n - 1$  ( $n = \text{integer}$ ; corresponding to one layer of ions for every  $n$  graphene layers) of the  $\text{AlCl}_4^-$  intercalated SPG compound<sup>44,45</sup>.

This means at stage-4 during charging  $> 2$  V, when  $\text{AlCl}_4^-$  ions intercalate into graphite, they force the layers apart, leading to a new reflection at  $20.7^\circ$ , caused by periodically inserted  $\text{AlCl}_4^-$  ions. At the same time, a partial peak shift towards higher angles results from the compression of non-intercalated layers.

Figure 3 b shows the changes in diffraction pattern over time during charging and discharging over 14 cycles. A repetitive pattern can be observed during discharging; however, it does not return exactly to its pristine state, probably due to residual disorder.

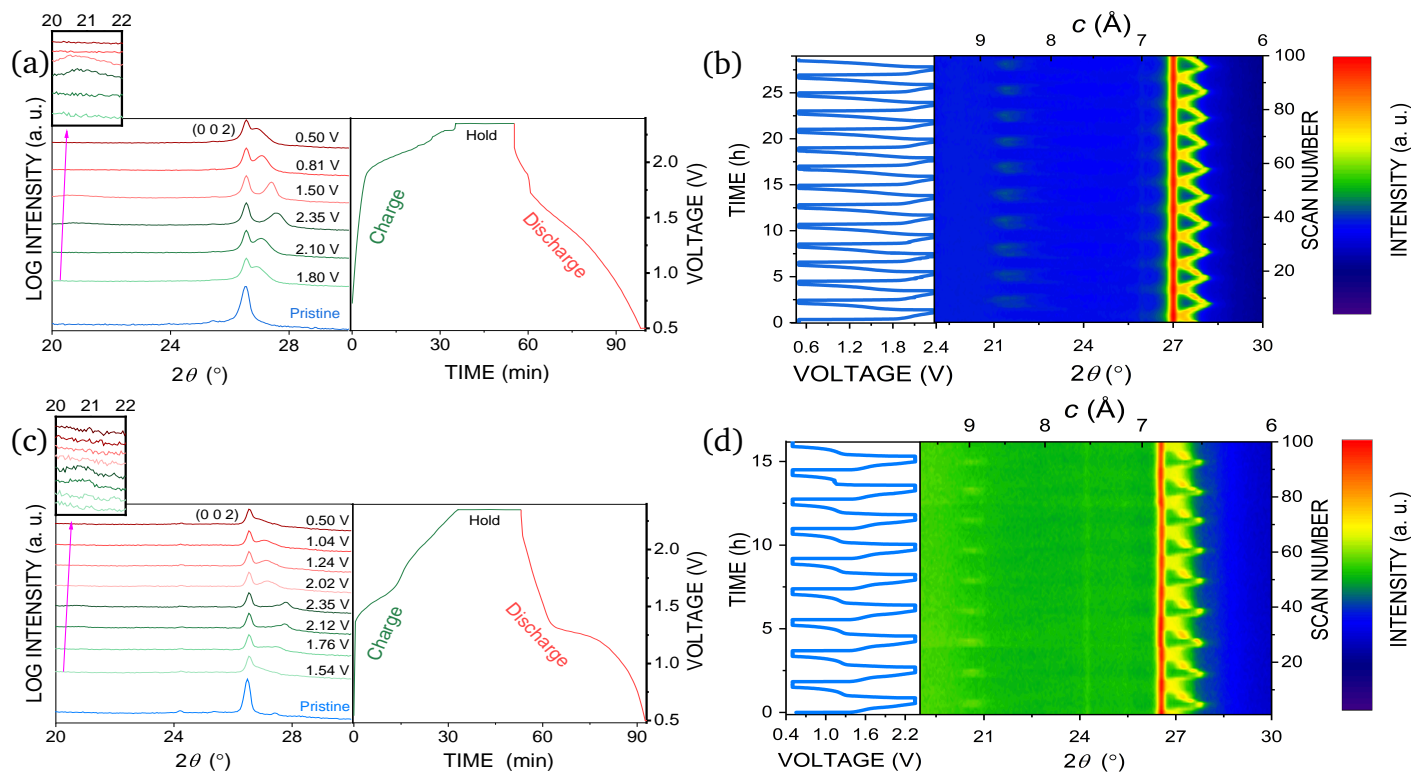


**Fig. 3** Operando XRD study of  $\text{AlCl}_4^-$  intercalation: a) diffraction patterns of a cell with SPG cathode combined with voltage time curve for 5<sup>th</sup> cycle, inset: zoom-in of the reflection at  $2\theta = 20^\circ - 22^\circ$ , b) contour plot of the same cell for 14 cycles with the changes in  $c$ -axis of the graphite structure, c) diffraction patterns of a cell with SPGPQ composite cathode with voltage-time curve, inset: zoom-in of the peak at  $2\theta = 20^\circ - 22^\circ$  and d) contour plot of the same cell for 9 cycles with the changes in  $c$ -axis of the graphite structure.

der and strain, which could be attributed to an irreversible reaction process. Although the peak intensity at  $26.6^\circ$  is reduced at the end of charging, it is still dominating. The partial but consistent peak shifting towards higher angles for every charged state (2.35 V) and returning to its initial state at 0.5 V indicates a high degree of reversibility of the intercalation-deintercalation process even though the graphite structures were not restored completely. The structural analysis also suggests a continuous structural compression and elongation along the  $c$ -axis from 6.4 Å (charging) to 6.7 Å (discharging), which is similar to previous studies<sup>30,43</sup>.

In Figure 3 c, the diffraction pattern of the SPGPQ composite cathode during cell cycling is shown. The organic PQ does not show any distinct diffraction peaks other than the characteristic peak of graphite at  $26.6^\circ$ . This indicates that the complexation of PQ with  $\text{AlCl}_3$ -based ions has converted PQ to an amorphous phase. From the FT-IR analysis, it is observed that complexation reactions take place between  $\text{C}=\text{O}$  of PQ and  $[\text{AlCl}_x]^{3-x}$  when they come into contact, which could result in such an amorphous state (see Figure 3 c and d). Therefore, the crystallinity of PQ likely does not play a significant role in the electrochemical process. In addition, the amorphization of PQ could be advantageous in resisting phase transition and dissolution, and enhancing stability, which implies enhanced cyclability<sup>20,22</sup>. Although the intensity of the graphite 002 reflection in SPGPQ is weaker than for the pure SPG cathode, a similar trend of peak shifting and new peak emerging is observed during cycling. This strongly supports the hypothesis of the graphite contributing to electrochemical re-

actions (intercalation) also for composite cathodes. In this case, the peak shifts to a slightly higher angle of  $27.8^\circ$  compared to the SPG cathode with  $27.6^\circ$ . The stable reversibility of intercalation-deintercalation can also be confirmed from Figure 3 d, i.e. the composite cathode behaves similar to SPG.

### 2.3.2 FT-IR analysis

Like all  $n$ -type compounds that accept electrons and become negatively charged during discharge,  $\text{C}=\text{O}$ , the electroactive functional group of PQ, is reduced during discharge and interacts with  $\text{Al}_2\text{Cl}_7^-$ . There are different opinions in the literature about the coordinating chloroaluminate complexes, for example,  $\text{AlCl}_2^+$ <sup>20,46,47</sup> and  $\text{AlCl}^{2+}$ <sup>19,23,42</sup>, which influences the achievable capacity of the cathodes accordingly. To investigate the reaction mechanism, ATR-FTIR spectroscopy is carried out on different states of the solid polymer RABs with SPGPQ cathodes. In this case, the IR spectra of pristine SPGPQ and cells after charge-discharge, discharge-charge-discharge, after the first charge and the 25<sup>th</sup> charge are recorded (see Figure 4) to have a clear understanding of the mechanism and reversibility.

The spectrum of the pristine SPGPQ composite is dominated by the stretching vibrations and bending vibrations of the ring compound consisting of  $\text{C}=\text{C}$  and  $\text{C}-\text{H}-\text{C}$  groups. The stretching vibration of the carbonyl bond  $\text{C}=\text{O}$ , the characteristic mode of quinone is found at  $1673\text{ cm}^{-1}$ <sup>48</sup>. After the first charge (2.35 V), the characteristic peak at  $1673\text{ cm}^{-1}$  disappears and a new broad and dominant peak appears at  $1536\text{ cm}^{-1}$  (see Figure 4 b), which



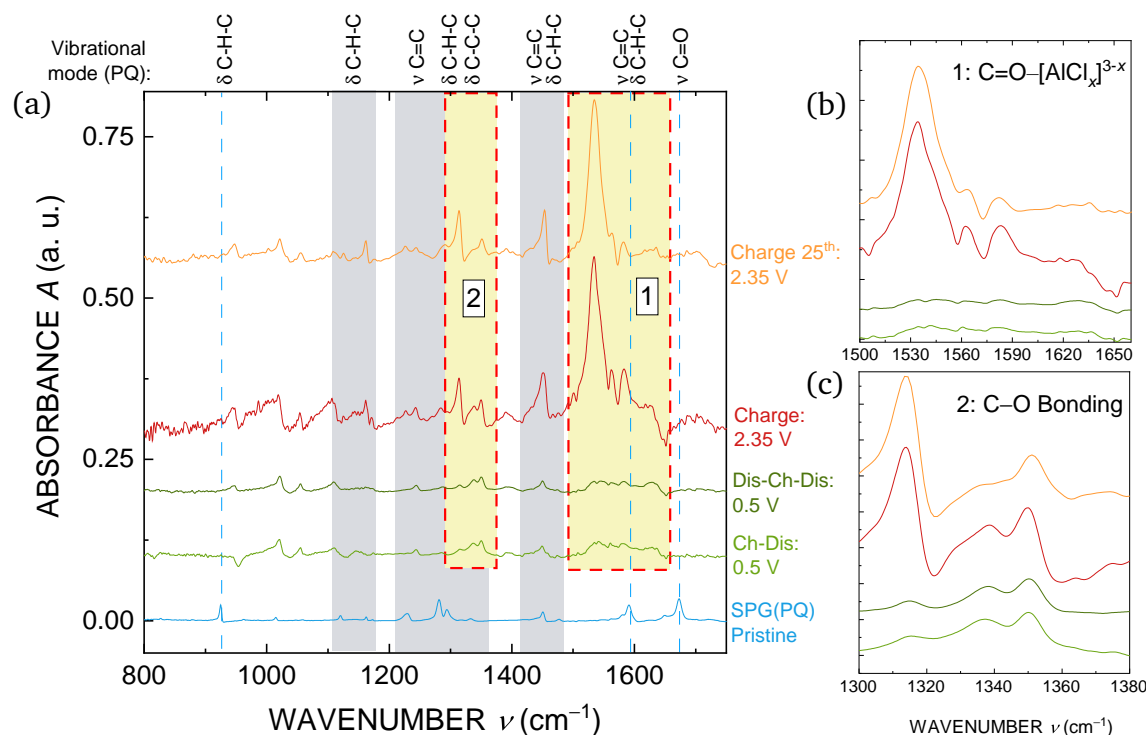


**Fig. 4** FTIR spectra of the SPGPQ composite at different states of cycling: a) full spectra, b) magnified portion for  $\text{C}=\text{O}-[\text{AlCl}_x]^{3-x}$  complexation and c) magnified portion for C-O formation during discharging.

can be attributed to the interaction between the electroactive carbonyl group and the  $\text{Al}_2\text{Cl}_7^-$ . This could be the stretching vibration of a new complex of the carbonyl group  $\text{C}=\text{O}-[\text{AlCl}_x]^{3-x}$  ( $0 < x < 3$ ). A couple of other peaks observed around  $1314\text{ cm}^{-1}$  can also be attributed to such complexation<sup>19</sup> (see Figure 4 c).

Both the discharged spectra at a voltage of 0.5 V show a distinct difference compared to the charged state. The vibrational modes at  $1536\text{ cm}^{-1}$  and  $1314\text{ cm}^{-1}$  entirely disappear and a doublet of new vibration modes at  $1337\text{ cm}^{-1}$  and  $1350\text{ cm}^{-1}$  increase prominently, which can be assigned to the stretching vibration of C-O (see Figure 4 c)<sup>23</sup>. This phenomenon suggests that the interactions between the C=O group of quinone and  $\text{AlCl}_x$  complexes change the vibrational modes and never return to their initial state. The new peaks at  $1337\text{ cm}^{-1}$  and  $1350\text{ cm}^{-1}$  reflect the electron transfer process during discharge, where C=O is reduced to C-O.

Furthermore, the spectrum of a charged cathode after the 25<sup>th</sup> cycle produced almost a similar spectrum to the charged cathode after the first charge indicating the high reversibility of the complexation reaction. The ratio of the integrated area of the broad peaks at  $1536\text{ cm}^{-1}$  (see Figure 4 b) of the two charged states is  $\approx 94\%$ , which also suggests a highly reversible complexation process with minimal irreversibility. This observation highlights the consistent appearance of the peak for  $\text{C}=\text{O}-[\text{AlCl}_x]^{3-x}$  complexation while charging and decomplexation during discharging after multiple charge and discharge cycles. The slight decrease in the integrated area could be caused by some minor side reactions or slow decomposition of PQ and SPGPQ. However, the analysis evidently supports that the core electrochemical processes are

highly reversible, which is crucial for the long-term stability and efficiency of the battery.

### 2.3.3 X-ray photoelectron spectroscopy (XPS) analysis

The XPS peak shift provides practical insight into the binding structures of the charge carrier ions. This is due to the sensitivity of the binding energy of the core electrons to the chemical environment of the corresponding element. For this, *ex-situ* XPS measurements of pristine, fully charged and fully discharged SPGPQ cathodes were performed. It is noteworthy that all XPS peaks were referenced relative to the C-C bond at 284.8 eV in the C 1s branch. The individual spectra of O 1s, C 1s, Al 2p and Cl 2p with fitting curves are illustrated in Figure 5. Figure S2 in the electronic supporting information (ESI<sup>†</sup>) shows the survey spectra and pristine O 1s and C 1s. The O 1s spectrum of the pristine SPGPQ (see Figure S2 c) is deconvoluted into peaks at 532.3 eV, 533.7 eV and 534.3 eV, which can be assigned to C=O (carbonyl group of PQ), C-O, and C-OH<sup>19,49</sup>. The carbonyl group is dominating in the charged state and decreasing significantly, when completely discharged (see Figure 5 a). This can be attributed to the formation of  $\text{C}=\text{O}-[\text{AlCl}_x]^{3-x}$  through a coordination reaction. The fully charged state exhibits slightly broader peaks compared to the pristine state (see Figure S2 c) probably due to the presence of  $\text{AlCl}_x$  species, i.e.  $\text{C}=\text{O}-[\text{AlCl}_x]^{3-x}$ . This is in agreement with the FT-IR results in the previous section.

Significant changes are observed in the C 1s spectra. Spectra in the pristine sample (see Figure S2 b, ESI<sup>†</sup>) do not have any shoulder or doublet, where C=O or C-C, C-O, C-H and C=O would be located at 284.7 eV, 285.6 eV, 286.9 eV and 288.6 eV, respectively<sup>21,50</sup>. The charged state develops a broader and more



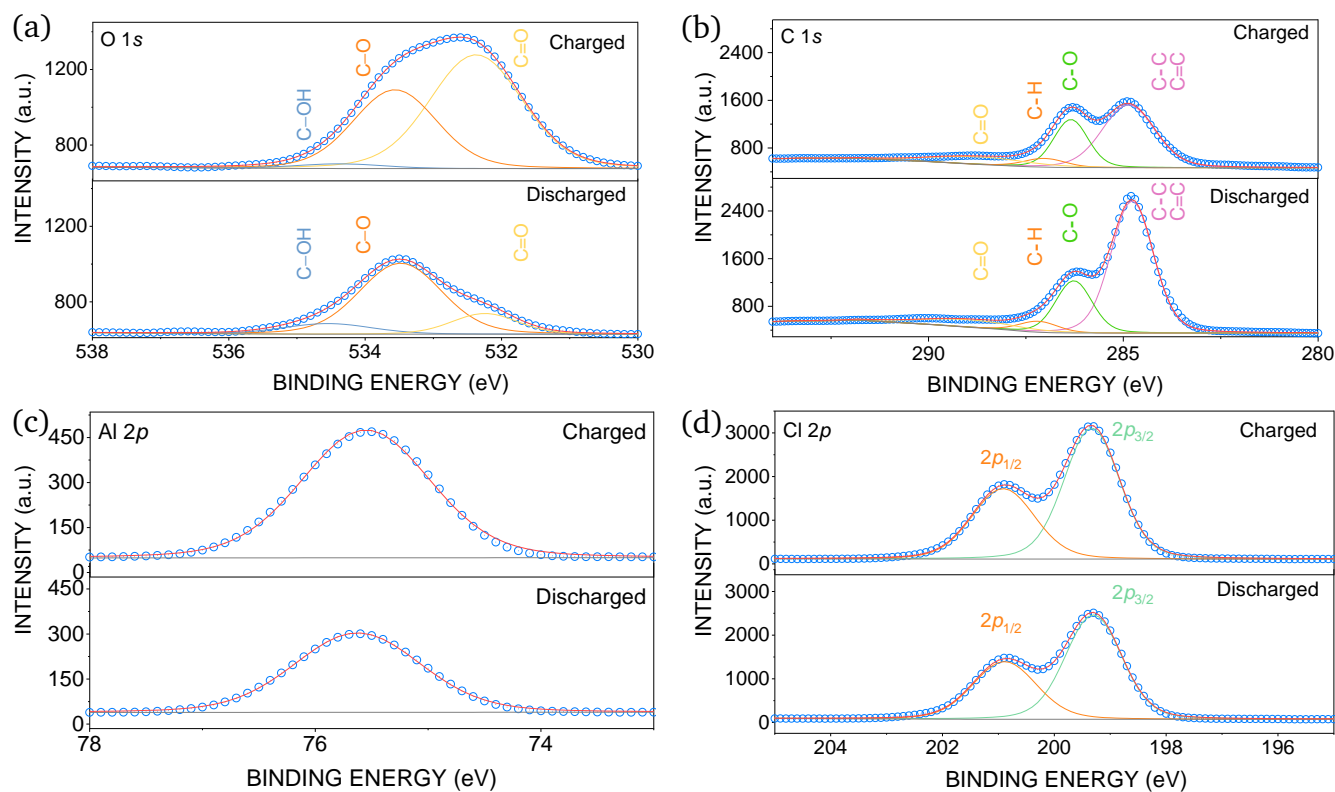


Fig. 5 XPS spectra of elements for charged and discharged state of the SPGPQ cathode with fitting curve: a) O 1s, b) C 1s, c) Al 2p and d) Cl 2p.

prominent shoulder at a higher binding energy of 286.3 eV. This could be a result of the electrochemical oxidation of graphite by the intercalation of  $\text{AlCl}_4^-$ <sup>29</sup>, which is reduced when discharged (see Figure 5 b). However, it does not return to its initial state.

More insights into ion species can be obtained from the Cl 2p (199.3 eV for  $2p_{2/3}$  and 200.9 eV for  $2p_{1/3}$ ) and Al 2p (75.6 eV) spectra, where the intensity in the charged state was significantly higher than the discharged state. The calculated atomic concentration ratios of Al and Cl are approximately 1:4 in the charged state and 1:2.2 in the discharged state. These ratios suggest that  $\text{AlCl}_4^-$  species dominate in the charged state, which is consistent with the intercalation of  $\text{AlCl}_4^-$  into graphite layers. In the discharged state, the possible ionic compound is  $\text{AlCl}_2^+$ , indicating the coordination reaction accompanied by a one-electron transfer process, likely involving the formation of  $\text{C}=\text{O}-[\text{AlCl}_x]^{3-x}$  complexation. Energy dispersive X-ray spectroscopy (EDS) analysis at multiple points (see Figure S3, ESI<sup>†</sup>) reveals atomic ratios of 1:3.8 in the charged state and 1:2.0 in the discharged state, as shown in Table S2 (ESI<sup>†</sup>), further corroborating this finding. A similar ratio is also reported by Yoo et al.<sup>21</sup> and Mao et al.<sup>47</sup>.

### 2.3.4 Electron spin resonance (ESR) analysis

ESR spectra of the samples were recorded, as depicted in Figure 6. All treated composites and the pristine state exhibit a signal close to the free electron of approximately  $g_e = 2.004$ . The untreated SPGPQ composite displays only a very weak signal, which possesses the well-known shape of graphitic material with its anisotropic  $g_e$  value (see Figure 6 inset)<sup>51</sup>.

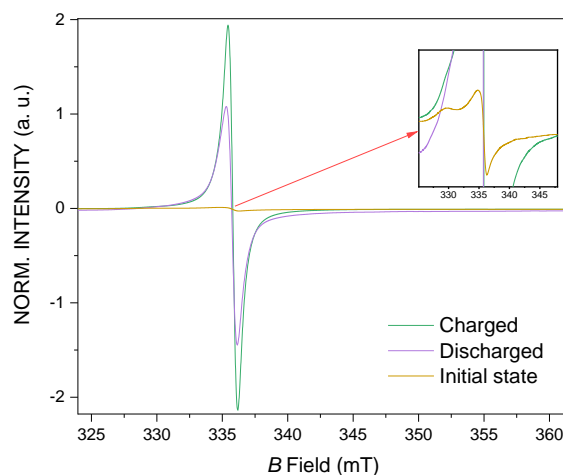


Fig. 6 ESR analysis of initial, charged and discharged state of an SPGPQ cathode normalized to sample mass, inset: a magnified view of the initial state spectrum.

Conversely, the loaded and unloaded composite materials exhibit a large signal, attributable to the accommodation of charges. During the charging process,  $\text{AlCl}_4^-$  is intercalated into the graphite; due to the reversibility of this process, this signal should be significantly reduced upon discharging. However, this is not the case, but almost an equally large area (3.8992 at 2.35 V after fully charged and 3.6429 at 0.5 V after fully discharged) under the ESR signal is detected. This confirms the FTIR results, indicating the formation of radical states due to complex-



ation processes involving the carbonyl group of PQ upon contact with the electrolyte. Both the  $\text{C}=\text{O}-[\text{AlCl}_x]^{3-x}$  complexation and  $\text{C}-\text{O}-\text{AlCl}_2^+$  coordination are ESR-active. In the discharged state, only one electron per molecular unit of PQ is available, which explains the resulting spectral shape. This means the one-electron transfer process of PQ is preferable, which is also supported by the XPS analysis<sup>20,22</sup>.

## 2.4 Electrochemical analysis

### 2.4.1 Reaction kinetics

Figure 7 a shows the CV curves comparing PQ, SPG, and SPGPQ at a scan rate of 1 mV/s, where the specific (sp.) current density is calculated using the active mass of the cathode. The CV curves have multiple oxidation and reduction peaks, and the composite offers a significantly higher sp. current density compared to its components. In the case of SPGPQ, the peaks are merged, suggesting that both graphite and PQ contribute synergistically to the electrochemical reaction kinetics, similar to previously reported PQ composites<sup>20</sup>. This merging of peaks in SPGPQ enables the possibility of a wider voltage window for charging and discharging, which is advantageous for enhanced battery performance. When comparing the peak positions across all curves, it becomes evident that the fabricated composite offers a wider functional charge-discharge window (2.35 V – 0.5 V) compared to PQ (1.8 V – 0.2 V) and SPG (2.35 V – 0.8 V).

Notably, the primary oxidation peak of SPGPQ occurs at 1.6 V with a sp. current density of  $\approx 240$  mA/g, while the correspond-

ing reduction peak is observed at  $\approx 1.2$  V with a higher sp. current density of 364 mA/g. The ratio of the reduction (190.7 V-mA/g) and oxidation (188.4 V-mA/g) area is nearly 1, which suggests excellent reversibility with high efficiency. The composite also has a remarkably higher integrated CV area (423.6 V-mA/g) than the sum of CV areas of its components (263.3 V-mA/g). The calculated capacity of SPGPQ cathode based on the integrated area is 1.6 times higher than the combined capacity (see Figure 7 a). Such an increase in CV capacity could be attributed to the synergistic contribution of its components.

In addition, the increased surface area due to changes in shape and surface morphology during annealing (see Figure 1 d) may also result in more active sites for electrochemical reactions. This enhanced surface area would facilitate better ion accessibility and shorter diffusion pathways, resulting in efficient charge storage and higher capacity. The significantly increased conductivity of the composite electrodes (1.36 S/m) compared to PQ (0.56 S/m) (see Table 1) suggests better electrical pathways and reduced resistance, which ensures faster electron transfer. This also decreases the energy loss, supporting higher current density and contributing to a higher overall performance.

A scan rate-dependent CV measurement of a full RAB with SPGPQ cathode was carried out from 1 mV/s to 4 mV/s (see Figure 7 b) to elucidate the current contributions. The peak currents increased gradually with increasing sweep rate, with a slight peak shift from 1.67 V at 1 mV/s to 1.73 V at 4 mV/s (anodic) and from 1.14 V at 1 mV/s to 1.06 V at 4 mV/s (cathodic), while peak shapes remained unchanged. This phenomenon can be attributed

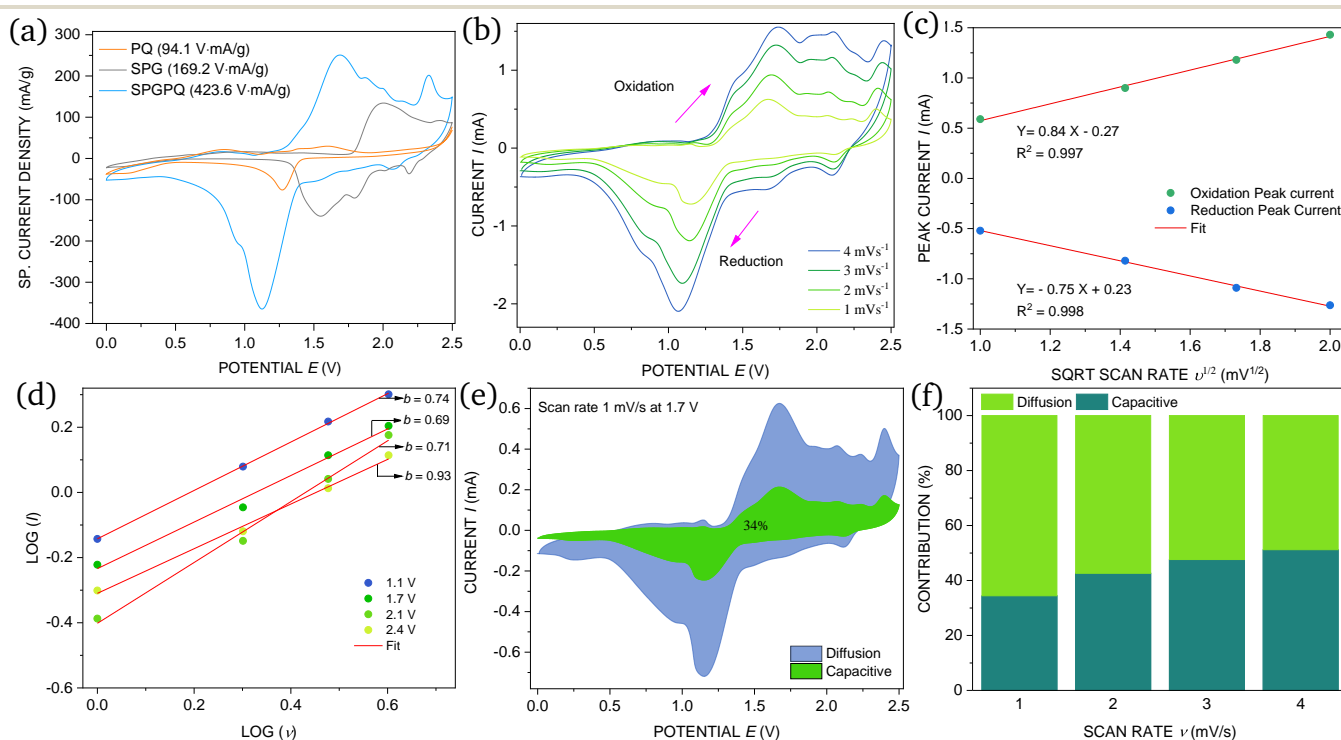


**Fig. 7** Reaction kinetics analysis of the composite electrodes: a) comparison of CV curves between SPGPQ and its components at 1 mV/s with integrated area given in the legend, b) scan-rate dependency of the composite cathode, c) the relation between peak currents and the square root of scan rates, d) calculation of  $b$  values at different peak positions, e) contribution of capacitive and diffusion current at 1 mV/s, and f) current contribution at different scan rates.



**Table 1** Electrode conductivity and performance of different cathodes with only SPE at 25 mA/g

Cathode	Conductivity SD (S/m)	$\pm$	Maximum $C_{\text{cathode}}$ (mAh/g)	Capacity retention (% after cycle 75)	Coulombic efficiency (% after cycle 75)	Energy Density (Wh/kg)
PQ	0.56 $\pm$ 0.02		45.6	70	44	64
SPG	5.43 $\pm$ 0.80		47.4	99	99	66
GFPQ	1.24 $\pm$ 0.04		88.0	87	90	119
SPGPQ	1.36 $\pm$ 0.04		79.2	99	99	111
MCMBPQ	0.92 $\pm$ 0.08		86.4	87	97	121

to a partial diffusion-controlled current with mostly reversible behavior. Peak currents are proportional to the square root of the sweep rate with an impressive  $R^2$  value  $> 0.99$  for both anodic and cathodic reactions, which suggests high reversibility (see Figure 7 c). Further analysis using the power law

$$i = a\nu^b \quad (2)$$

at different peak positions and constant voltage shows that the  $b$  values differ from 0.7 to 0.9 (see Figure 7 d). Here,  $i$  is current,  $\nu$  is scan rate and  $a$ ,  $b$  are adjustable constants<sup>52</sup>. There are two well-defined conditions, where  $b = 0.5$  signifies an ideal diffusion-controlled current contribution and  $b = 1$  represents an ideal capacitive response. Therefore, the  $b$  value between 0.7 and 0.9 means the RAB with SPGPQ is a partial diffusion-controlled system, which is similar to pure PQ and also well-aligned with Yoo et al.<sup>22</sup>. To separate the individual contributions to the reaction kinetics a simplified equation

$$i = k_1\nu + k_2\nu^{1/2} \quad (3)$$

is used, where  $k_1\nu$  is capacitive current and  $k_2\nu^{1/2}$  is diffusion controlled current<sup>52</sup>. Figure 7 e indicates that, at a scan rate of 1 mV/s, the diffusion current contributes 66 % of the total current, with the remaining 34 % attributed to the capacitive current. However, as the scan rate increases, the capacitive current gradually rises from 34 % to 48 % (see Figure 7 f), signifying accelerated reaction kinetics<sup>53,54</sup>.

#### 2.4.2 Battery performance

RAB coin cells with composite, pure PQ, and SPG cathodes were cycled at 25 mA/g to evaluate the improvement of the SPGPQ performance compared to its components (see Figure 8 a). The cut-off charging and discharging voltages were set based on the CV analysis and the specific capacity is calculated considering the mass of active material of the cathode (see Table S1, ESI<sup>†</sup>). SPGPQ offers a capacity of 80 mAh/g, which is higher than the individual component capacity of PQ (46 mAh/g) and SPG (48 mAh/g).

However, the theoretical capacity of SPG (70 mAh/g) and PQ (129 mAh/g, for 1 electron process and 257 mAh/g for 2 electron process) mentioned in the supporting information<sup>†</sup> are much higher than the experimental values. The discrepancy could be due to the partial inactivity of the active materials during cycling of the batteries with SPE. Moreover, the lower ionic conductivity

of the SPE (0.3 mS/cm)<sup>38</sup> than the IL (12 mS/cm)<sup>55</sup> could be an influencing factor.

To test the hypothesis, different aluminum polymer batteries were cycled with ionic liquid wetted cathodes under similar conditions, ensuring the better utilization of the active materials. In this case, 5  $\mu$ L of 2:1 AlCl<sub>3</sub>/Et<sub>3</sub>NHCl IL were used to wet each of the cathodes before cycling at 25 mA/g. The results, shown in Figure 8 b, exhibit significantly higher capacities for all of the cathodes, with near theoretical values of SPG and PQ cathodes. These results validate the hypothesis that wetting of the cathodes enhances active material utilization. However, the capacity of the wet PQ cathode with SPE dropped drastically after the first cycle compared to the cell without wetting (see Figure S4, ESI<sup>†</sup>) due to faster dissolution of PQ<sup>19</sup>. Although the wet SPG cathode offers slightly better capacity, CE decreases to 90 % (see Figure S4 c, ESI<sup>†</sup>), which is lower than that of the cell with only SPE. A similar trend is observed for the wet composite cathode. Both the composite and its components offer poor cyclability when the cathodes were wet.

A closer inspection of the plateau of the curves in Figure 8 a reveals a synergistic effect in the case of SPGPQ. After a sharp increase of the voltage from 0.5 V to 1.7 V, SPG offers a broad and gradual charge plateau (grey curve), which starts at 4 mAh/g and increases to 47 mAh/g during charging, suggesting the intercalation of AlCl<sub>4</sub><sup>-</sup>. On the other hand, the discharge voltage is around 1.8 V as the capacity approaches 46 mAh/g until the cut-off voltage of 0.5 V. PQ shows a much more stable plateau (1.4 V 1.2 V) throughout its capacity until a sudden voltage drop at around 44 mAh/g during discharge is caused by concentration polarization and over-potential<sup>56</sup>. The voltage of PQ during charging reaches its cut-off voltage at a steady pace.

The composite (blue curve) follows both of the trends. It starts its plateau at around 1.4 V and imitates the consistent behavior of PQ delivering a specific capacity of 44 mAh/g during charging. At 1.7 V, it has a similar pattern to pure SPG with an extended capacity of 80 mAh/g. The combined properties are also well visible during discharging. Moreover, there is no sharp fall in capacity like for PQ cathodes; rather it reaches its cut-off voltage more steadily from 50 mAh/g at 1.3 V to 80 mAh/g at 0.5 V. Therefore, the composite incorporates the advantages of both SPG and PQ, resulting in improved performance and efficiency.

Based on CV and GCPL results, it is evident that both of the components are actively taking part in the electrochemical pro-



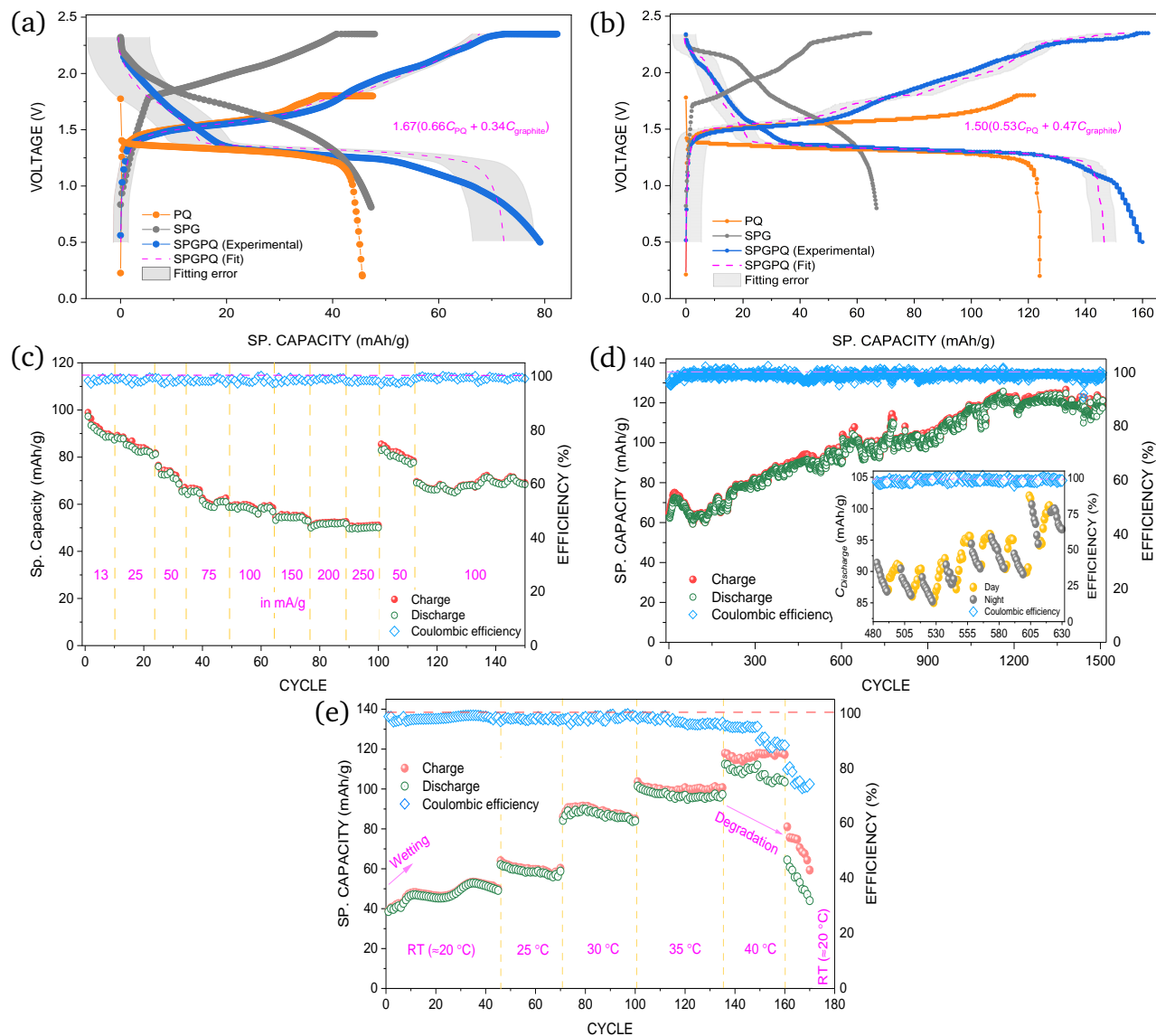


**Fig. 8** Electrochemical performance of SPGPQ cathodes: a) voltage profile of SPGPQ and its components over capacity with fit, b) discharge capacities and fit with wetted cathodes, c) rate-capability of capacity at different current densities, d) capacities and Coulombic efficiency over cycle number; inset: fluctuation in discharge capacity during day and night, and e) temperature dependency on the capacity at 180 mA/g.

cesses. The XRD analysis and spectroscopic results (XPS, FTIR, ESR) also support that both intercalation and coordination reaction are happening synergistically. To quantify the contribution of PQ and SPG to the composite overall capacity, a curve-fitting approach is employed using a simple linear combination model as a function of voltage:

$$C_{SPGPQ} = y \cdot [x \cdot C_{PQ} + (1 - x) \cdot C_{SPG}] \quad (4)$$

Here  $x$  signifies the fractional contribution of PQ,  $(1 - x)$  is the contribution of SPG, and  $y$  is a performance enhancement factor describing the synergistic effects in the composite. The fitting analysis predicts the charge and discharge capacities of SPGPQ with SPE to be 72 mAh/g, having an average of  $\bar{x} = 0.660 \pm 0.011$  and  $\bar{y} = 1.668 \pm 0.009$  (see Figure 8 a). The enhancement factor suggests that the composite fabrication activates one or both components, potentially enhancing the kinetics and improv-

ing utilization of active sites or ion diffusion pathways. The results demonstrate a firm alignment with the fitting values derived from the RABs having wetted cathodes (see Figure 8 b), where  $\bar{x} = 0.526 \pm 0.007$  and  $\bar{y} = 1.502 \pm 0.014$ , thereby validating the methodological approach employed. The details of the fractional contribution of PQ ( $x$ ) and enhancement factor ( $y$ ) are presented in the electronic supporting information (ESI<sup>†</sup>), Table S3. Changes in  $x$  may influence the specific capacity. Higher  $x$  values could shift the charge-discharge plateau toward that of PQ, while lower  $x$  values may align it more closely with SPG. Such adjustments could provide a balance between capacity, cyclability, and structural integrity of the composite.

Furthermore, the analysis indicates that PQ and SPG contribute to the SPGPQ capacity at a fractional ratio  $x/(x - 1)$  of 1.1 – 1.9. While this ratio differs from the composite's molar ratio of 2.77:1 (see supporting information), it could reflect an underlying re-



relationship between the electrochemical contributions and the composition. Furthermore, the performance enhancement factor ( $\gamma > 1$ ) is consistently observed across all cases, supporting the notion of synergy and the amplified performance of the composite.

To analyze the battery performance at different current densities, an RAB coin cell was cycled from 13 mA/g to 250 mA/g (see Figure 8 c). The battery exhibits the typical trend of decreasing capacity with increasing current density, as higher charging and discharging rates (e.g. 250 mA/g) result in kinetic limitations such as slower ion diffusion and increased polarization effects. Despite these challenges, the composite cathode sustained a capacity of 80 mAh/g at 50 mA/g after returning from 250 mA/g. The high Coulombic efficiency of  $(99 \pm 2) \%$ , along with this capacity recovery, demonstrates the battery's impressive rate capability and reversibility. At the highest tested current density of 250 mA/g, the battery maintained a capacity of  $\approx 51$  mAh/g, retaining approximately 56 % of its low-rate capacity (91 mAh/g at 13 mA/g). Moreover, the capacity recovery to 80 mAh/g at 50 mA/g and 68 mAh/g at 100 mA/g after the current density was reduced further suggests that the composite material remained stable during higher-rate cycling. This indicates that the capacity loss observed at higher rates is primarily due to kinetic limitations rather than irreversible damage to the battery.

Figure 8 d shows the cyclability of a solid polymer RAB with composite cathode at a current density of 210 mA/g for charging

and 175 mA/g for discharging. The initial capacity was 61 mAh/g, which kept increasing over cycling and reached 122 mAh/g at cycle 1500 with a high Coulombic efficiency of  $(99 \pm 1) \%$ . The capacity was not stable but rather had a zigzag trend. This continuously increasing trend in capacity along with the high efficiency indicates the system is probably undergoing some activation processes with a larger over-potential or environmental influences. This type of activation process during the initial charging and the gradual increase in capacity is also mentioned in the case of PQ composite with activated carbon<sup>22</sup>. In addition, the use of solid ionic-polymer electrolytes may also crucially limit cathode wetting. This means, over the cycles more and more composite material becomes accessible to the electrolyte thereby increasing capacity. There is a small drop of capacity after the 35<sup>th</sup> cycle, which could be a result of a stabilization phase at the electrode-electrolyte interface, i.e. the system reaches a saturation state.

Other possible reasons could be unwanted side reactions with the moisture content present in the deeper layers of the cathodes or initial dissolution of PQ limited to a certain proportion. However, the consistent CE of 99 % suggests that such unwanted reactions or dissolution are very limited. Apart from these, the ambient temperature can also be a critical parameter. An increasing pattern in  $C_{\text{cathode}}$  during the day and a decreasing trend during the night (see the inset of Figure 8 d) suggest the vital role of temperature. It is important to note that the temperature in-

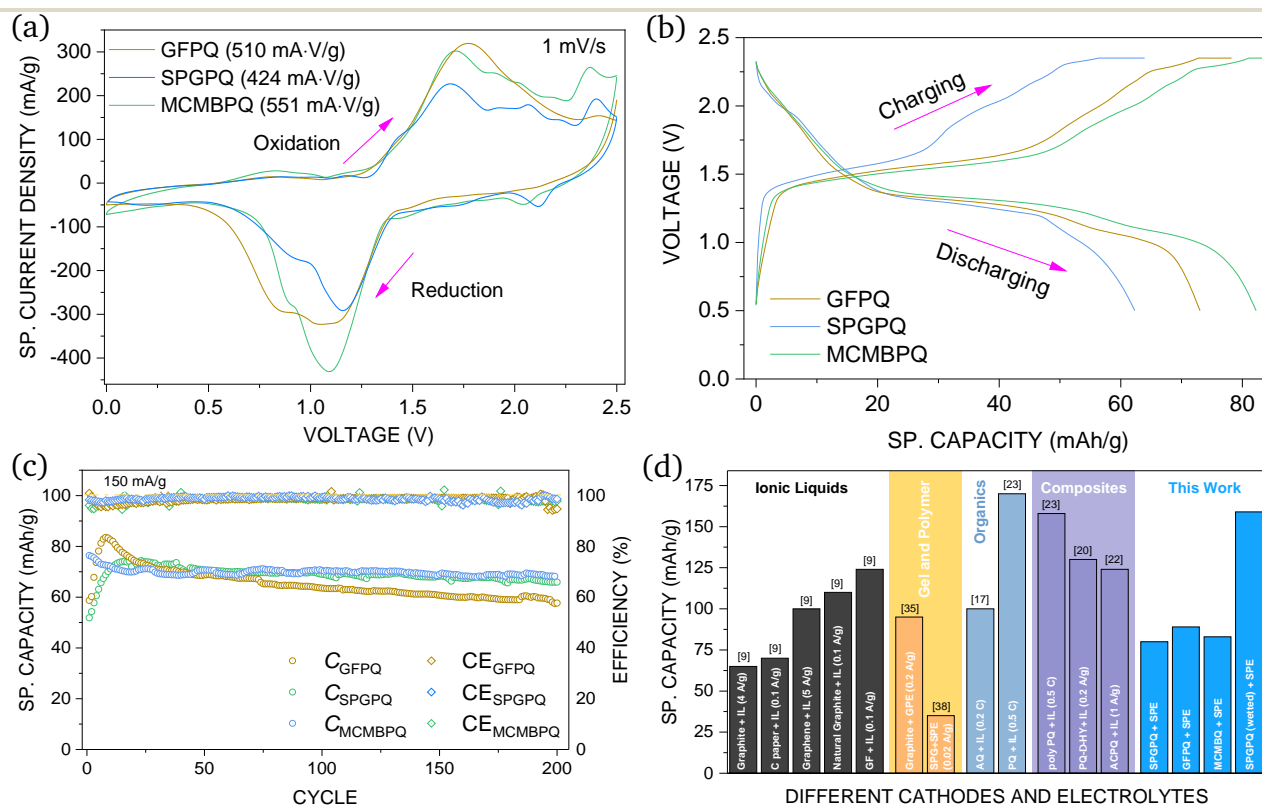


**Fig. 9** Electrochemical performance of composite cathodes with different shapes of graphites: a) comparison of CV curves, b) Galvanostatic voltage profile of different composite cathodes at 50 mA/g, c) total capacity and Coulombic efficiency of the RABs with different cathodes and d) a comparison of capacity between composites studied in this work and previously reported cathodes.

creased from 22 °C to 31 °C during the cycling. An increase in temperature can enhance ion mobility and reduce cell resistance resulting in a capacity increase, however, the consistent and high Coulombic efficiency ensures that there is no significant degradation inside the cell and the composite remains stable at least in a certain temperature range.

To verify the temperature sensitivity and identify the operating range, a temperature-controlled GCPL was carried out at 225 mA/g. For each temperature increase, there was a 2-hour resting period to allow the cell to adapt to the new temperature. There is a distinct trend of increasing capacity with increasing temperature suggesting that the system is severely sensitive to temperature. Figure 8 e shows that the initial capacity is around 40 mAh/g, which increases up to 53 mAh/g until the 35<sup>th</sup> cycle at room temperature. The observed trend could be attributed to enhanced cathode wetting with SPE, leading to improved accessibility of the solid electrolyte to the active material. The capacity reaches 90 mAh/g at 30 °C and 102 mAh/g at 35 °C following a consistent pattern due to enhanced ionic conductivity and improved electrode kinetics. Additionally, the increased fluidity of the SPE at elevated temperatures likely facilitates cathode wetting, enabling better utilization of the active material in the electrochemical reaction.  $C_{\text{SPGPQ}}$  returns to its initial value when the temperature is lowered back to room temperature further confirming the temperature sensitivity of the cell. The system maintains a high CE of  $(98 \pm 2) \%$  up to 35 °C, which indicates a high reversibility in this temperature range and the increased capacity does not come at the cost of efficiency. However, despite the high capacity at 40 °C, a gradual decrease in CE suggests the initiation of side reactions and irreversible material degradation. These parasitic side reactions are possibly attributed to thermal degradation of the PA6-based polymer electrolyte, the onset of chemical decomposition of the PMMA binder, or partial dissolution of PQ under electrochemical stress at elevated temperatures. Upon returning to room temperature, the capacity reverted to its initial value; however, the persistent capacity fading signifies continued degradation. This observation indicates an optimal temperature limit of 35 °C and also confirms that the temperature influence was dominating while the cell was cycling (see Figure 8 d). In addition, the use of thermally stable solid polymer electrolytes, such as PAN-based systems<sup>57</sup> along with alternative binder additives and optimized graphite to PQ ratio, could help mitigate performance degradation at elevated temperatures ( $> 35$  °C).

### 2.4.3 Influence of the graphite shape

To analyze the shape dependency of the graphite host material on the composite cathode performance, different graphites, i.e. MCMB, GF, and SPG, were tried as hosts for the synthesis of composites using melt diffusion. Figure 9 a illustrates the CV curves of GFPQ, SPGPQ and MCMBPQ at 1 mV/s. All of the cathodes have almost identical curves with very similar peak shapes and positions. Although the specific current density of the SPGPQ peak is lower than for the other two, the patterns are similar. The specific capacity considering the integrated area of the SPGPQ (424 mA·V/g) was also lower than for both GFPQ (510 mA·V/g) and MCMBPQ (550 mA·V/g). The variations can be attributed to

the shape of the hosts and the process parameters. As mentioned earlier, the SPE may take some time to wet cathodes, which may vary from cell to cell.

The trend of increasing capacity observed in CV is also reflected in the charge-discharge voltage profile at a current density of 25 mA/g (see Figure 9 b). MCMBPQ offers the highest capacity of  $\approx 84$  mAh/g compared to GFPQ (79 mAh/g) and SPGPQ (63 mAh/g) after the 50<sup>th</sup> cycle. The plateaus during charging and discharging are also similar, indicating the improved performance of the composites regardless of the graphite type. However, when charging at a higher current density of 150 mA/g, the difference in capacities is reduced significantly with a promising CE  $(99 \pm 4) \%$  (see Figure 9 c). The influence of increased current density on SPGPQ is minimal, which can be attributed to its superior electrical conductivity of 1.36 S/m (see Table 1), facilitating faster electron transport and enabling more efficient electrical pathways. Table 1 presents the electrochemical performances of different composite cathodes. The capacity retention of all the composites is also improved up to 99 % compared to pure PQ (70 %) after 75 cycles (see Figure S4 a and 4b, ESI<sup>†</sup>). The energy density of the composite cathodes with SPE is also improved almost 100 % compared to both PQ and SPG.

A comparison of the initial discharge capacities for cathode materials from this study and literature is presented in Figure 9 d. The composite cathodes synthesized in this work achieve capacities up to 90 mAh/g with SPE, and 160 mAh/g, when wetted with an ionic liquid (IL). This performance confirms a significant improvement over conventional graphite cathodes paired with IL or SPE.

## 3 Conclusion

A composite consisting of PQ and graphite was synthesized using a simple one-step melt diffusion process for RABs, which was confirmed by several experimental observations, i.e. CBS, TGA, and XRD. The FTIR data analysis indicates that the composite is comparatively more stable than the pure PQ while its electrical conductivity is nearly twice as high, demonstrating a significant improvement.

In the electrochemical reaction process, two different ionic species are involved, which are the intercalation of  $\text{AlCl}_4^-$  into graphene layers during charging and coordination reactions between  $\text{C}=\text{O}$  and  $\text{AlCl}_2^+$  during discharging with a high degree of reversibility. To verify this hypothesis, *operando* XRD, ATR-FTIR, XPS and EPR measurements were carried out. All of the analyses support the hypothesis that two different reaction mechanisms are taking place simultaneously with impressive reversibility. The CV curve analysis confirms the peak merging, which is also congruent with the other findings.

The overall battery capacity of the composite cathode with SPE is significantly improved by more than 70 % compared to pure graphite and 82 % compared to PQ, which is consistently reproduced with two other forms of graphite. The experimental data also suggest that the iono-polymer RABs with a composite cathode can operate without degradation up to a temperature of 35 °C. All the composites can be cycled at a high current density of 250 mAh/g with an exceptional Coulombic efficiency of



(99 ± 2) %. Overall, the composite has high potential as an active material for safe and high-performance iono-polymer RABs.

## Author contributions

Shuvrodev Biswas contributed to the writing of the original draft, sample preparation and characterization, data processing, editing, investigation, and overall study design. Thomas Köhler was responsible for FT-IR and EPR investigations, data processing, editing, and experimental idea development. Amir Mohammad developed the electrolyte recipe and contributed to the research framework. Hartmut Stöcker participated in XRD analysis, review, editing, supervision, and project guidance. Dirk C. Meyer was involved in editing, validation, supervision, project administration, and funding acquisition.

## Conflicts of interest

There are no conflicts to declare.

## Data availability

Due to the large volume of calculation data in this paper and the data-sharing restrictions imposed by our institution, it is not possible to upload all datasets to a public repository. However, supplementary information<sup>†</sup> is provided, and additional data may be made available upon request.

## Acknowledgements

This work was funded by the Bundesministerium für Wirtschaft und Klimaschutz (BMWK, Federal Ministry for Economic Affairs and Climate Action) as a part of the project ProBaSol Die Aluminumbatterie: Herausforderungen für die industrielle Fertigung (03EI3014A). The authors gratefully acknowledge the financial support from the Deutsche Forschungsgemeinschaft (DFG, German Research Foundation) in collaboration with the Free State of Saxony for the large equipment application Digitales, höchstauflösendes FEG-Rasterelektronenmikroskop mit Focused Ion Beam Zusatz und Gas Injection System (INST 267/86-1 FUGG), which enabled us to acquire the SEM used for surface investigations. The authors thank U. Fischer and C. Funke for acquiring the SEM images and EDS data. Special thanks also go to B. Störr for her cordial cooperation in the TGA analysis and N. Leubner for his cordial assistance to interpret the XRD data.

## References

- B. Ng, P. T. Coman, E. Faegh, X. Peng, S. G. Karakalos, X. Jin, W. E. Mustain and R. E. White, *ACS Applied Energy Materials*, 2020, **3**, 3653–3664.
- E. A. Olivetti, G. Ceder, G. G. Gaustad and X. Fu, *Joule*, 2017, **1**, 229–243.
- R. Wang, H. Wang, H. Zhao, M. Yuan, Z. Liu, G. Zhang, T. Zhang, Y. Qian, J. Wang, I. Lynch and Y. Deng, *Energy Materials*, 2023, **3**, 300040.
- T. Leisegang, F. Meutzner, M. Zschornak, W. Münchgesang, R. Schmid, T. Nestler, R. A. Eremin, A. A. Kabanov, V. A. Blatov and D. C. Meyer, *Frontiers in Chemistry*, 2019, **7**, 268.
- J. Tu, W.-L. Song, H. Lei, Z. Yu, L.-L. Chen, M. Wang and S. Jiao, *Chemical Reviews*, 2021, **121**, 4903–4961.
- B. Zhang, W. Zhang, H. Jin and J. Wan, *ChemistrySelect*, 2023, **8**, e202204575.
- X. Wen, Y. Liu, A. Jadhav, J. Zhang, D. Borchardt, J. Shi, B. M. Wong, B. Sanyal, R. J. Messinger and J. Guo, *Chemistry of Materials*, 2019, **31**, 7238–7247.
- C. Legein, B. J. Morgan, F. Fayon, T. Koketsu, J. Ma, M. Body, V. Saroukanian, X. Wei, M. Heggen, O. J. Borkiewicz, P. Strasser and D. Dambournet, *Angewandte Chemie International Edition*, 2020, **59**, 19247–19253.
- E. Faegh, B. Ng, D. Hayman and W. E. Mustain, *Nature Energy*, 2020, **6**, 21–29.
- K. V. Kravchyk, S. Wang, L. Piveteau and M. V. Kovalenko, *Chemistry of Materials*, 2017, **29**, 4484–4492.
- S. Gu, H. Wang, C. Wu, Y. Bai, H. Li and F. Wu, *Energy Storage Materials*, 2017, **6**, 9–17.
- Y. Liu, S. Sang, Q. Wu, Z. Lu, K. Liu and H. Liu, *Electrochimica Acta*, 2014, **143**, 340–346.
- Z. Li, B. Niu, J. Liu, J. Li and F. Kang, *ACS Applied Materials & Interfaces*, 2018, **10**, 9451–9459.
- M. Chiku, H. Takeda, S. Matsumura, E. Higuchi and H. Inoue, *ACS Applied Materials & Interfaces*, 2015, **7**, 24385–24389.
- S. K. Das, T. Palaniselvam and P. Adelhelm, *Solid State Ionics*, 2019, **340**, 115017.
- B. Tan, S. Han, W. Luo, Z. Chao, J. Fan and M. Wang, *Journal of Alloys and Compounds*, 2020, **841**, 155732.
- Z. Huang, X. Du, M. Ma, S. Wang, Y. Xie, Y. Meng, W. You and L. Xiong, *ChemSusChem*, 2023, **16**, e202202358.
- D. Kong, T. Cai, H. Fan, H. Hu, X. Wang, Y. Cui, D. Wang, Y. Wang, H. Hu, M. Wu, Q. Xue, Z. Yan, X. Li, L. Zhao and W. Xing, *Angewandte Chemie International Edition*, 2021, **61**, e202114681.
- J. Bitenc, N. Lindahl, A. Vizintin, M. E. Abdelhamid, R. Dominko and P. Johansson, *Energy Storage Materials*, 2020, **24**, 379–383.
- D. J. Kim, D.-J. Yoo, M. T. Otle, A. Prokofjevs, C. Pezzato, M. Owczarek, S. J. Lee, J. W. Choi and J. F. Stoddart, *Nature Energy*, 2019, **4**, 51–59.
- D.-J. Yoo, M. Heeney, F. Glöcklhofer and J. W. Choi, *Nature Communications*, 2021, **12**, 2386.
- D.-J. Yoo and J. W. Choi, *The Journal of Physical Chemistry Letters*, 2020, **11**, 2384–2392.
- J. Bitenc, U. Koir, A. Vizintin, N. Lindahl, A. Krajnc, K. Pirnat, I. Jerman and R. Dominko, *Energy Material Advances*, 2021, **2021**, 9.
- J. Zhang, Y. Wu, M. Liu, L. Huang, Y. Li and Y. Wu, *Angewandte Chemie International Edition*, 2023, **62**, e202215408.
- H. Xu, T. Bai, H. Chen, F. Guo, J. Xi, T. Huang, S. Cai, X. Chu, J. Ling, W. Gao, Z. Xu and C. Gao, *Energy Storage Materials*, 2019, **17**, 38–45.
- C. Xu, S. Zhao, Y. Du, Z. Wang and J. Zhang, *Materials Letters*, 2020, **275**, 128040.



- 27 F. Jach, M. Wassner, M. Bamberg, E. Brendler, G. Frisch, U. Wunderwald and J. Friedrich, *ChemElectroChem*, 2021, **8**, 1988–1992.
- 28 H. Sun, W. Wang, Z. Yu, Y. Yuan, S. Wang and S. Jiao, *Chemical Communications*, 2015, **51**, 11892–11895.
- 29 M.-C. Lin, M. Gong, B. Lu, Y. Wu, D.-Y. Wang, M. Guan, M. Angell, C. Chen, J. Yang, B.-J. Hwang and H. Dai, *Nature*, 2015, **520**, 324–328.
- 30 J. Meng, X. Yao, X. Hong, L. Zhu, Z. Xiao, Y. Jia, F. Liu, H. Song, Y. Zhao and Q. Pang, *Nature Communications*, 2023, **14**, 3909.
- 31 J. Meng, X. Hong, Z. Xiao, L. Xu, L. Zhu, Y. Jia, F. Liu, L. Mai and Q. Pang, *Nature Communications*, 2024, **15**, 596.
- 32 X. Han, Y. Bai, R. Zhao, Y. Li, F. Wu and C. Wu, *Progress in Materials Science*, 2022, **128**, 100960.
- 33 P. Meng, Z. Yang, J. Zhang, M. Jiang, Y. Wang, X. Zhang, J. Luo and C. Fu, *Energy Storage Materials*, 2023, **63**, 102953.
- 34 Z. Yu, S. Jiao, S. Li, X. Chen, W. Song, T. Teng, J. Tu, H. Chen, G. Zhang and D. Fang, *Advanced Functional Materials*, 2018, **29**, 1806799.
- 35 Z. Liu, X. Wang, Z. Liu, S. Zhang, Z. Lv, Y. Cui, L. Du, K. Li, G. Zhang, M.-C. Lin and H. Du, *ACS Applied Materials & Interfaces*, 2021, **13**, 28164–28170.
- 36 X.-G. Sun, Y. Fang, X. Jiang, K. Yoshii, T. Tsuda and S. Dai, *Chemical Communications*, 2016, **52**, 292–295.
- 37 A. Mohammad, T. Köhler, S. Biswas, E. Brendler, B. Störr, H. Stöcker, F. O. R. L. Mertens and D. C. Meyer, *ACS Applied Energy Materials*, 2025, **8**, 2576–2587.
- 38 A. Mohammad, T. Köhler, S. Biswas, H. Stöcker and D. C. Meyer, *ACS Applied Energy Materials*, 2023, **6**, 2914–2923.
- 39 Z. Zhu, Y. Men, W. Zhang, W. Yang, F. Wang, Y. Zhang, Y. Zhang, X. Zeng, J. Xiao, C. Tang, X. Li and Y. Zhang, *eScience*, 2024, **4**, 100249.
- 40 S. S. Nair, T. Saha, P. Dey and S. Bhadra, *Journal of Materials Science*, 2020, **56**, 3675–3691.
- 41 R. D. Knuth, F. A. Knuth, G. K. Maron, C. W. Raubach, M. L. Moreira, P. L. G. Jardim, N. L. V. Carreno, E. C. Moreira, A. Gündel, I. T. S. Garcia and S. S. Cava, *Journal of Solid State Electrochemistry*, 2023, **28**, 2059–2070.
- 42 N. Lindahl, J. Bitenc, R. Dominko and P. Johansson, *Advanced Functional Materials*, 2020, **30**, 2004573.
- 43 G. A. Elia, N. A. Kyremateng, K. Marquardt and R. Hahn, *Batteries & Supercaps*, 2018, **2**, 83–90.
- 44 C.-J. Pan, C. Yuan, G. Zhu, Q. Zhang, C.-J. Huang, M.-C. Lin, M. Angell, B.-J. Hwang, P. Kaghazchi and H. Dai, *Proceedings of the National Academy of Sciences*, 2018, **115**, 5670–5675.
- 45 P. Bhauriyal, A. Mahata and B. Pathak, *Physical Chemistry Chemical Physics*, 2017, **19**, 7980–7989.
- 46 F. Guo, Z. Huang, M. Wang, W.-L. Song, A. Lv, X. Han, J. Tu and S. Jiao, *Energy Storage Materials*, 2020, **33**, 250–257.
- 47 M. Mao, Z. Yu, Z. Lin, Y.-S. Hu, H. Li, X. Huang, L. Chen, M. Liu and L. Suo, *Journal of Materials Chemistry A*, 2020, **8**, 23834–23843.
- 48 G. BARUAH, D. TRIPATHI and S. NATH, *Current Science*, 1970, **39**, 405–407.
- 49 P. Pal, H. Li, R. AlAjeil, A. K. Mohammed, A. Rezk, G. Melinte, A. Nayfeh, D. Shetty and N. ElAtab, *Advanced Science*, 2024, **11**, 2408648.
- 50 F. A. Stevie and C. L. Donley, *Journal of Vacuum Science & Technology A: Vacuum, Surfaces, and Films*, 2020, **38**, 063204.
- 51 J. Stankowski, L. Piekara-Sady, W. Kempiski, O. Huminiecki and P. B. Sczaniecki, *Fullerene Science and Technology*, 1997, **5**, 1203–1217.
- 52 J. Wang, J. Polleux, J. Lim and B. Dunn, *The Journal of Physical Chemistry C*, 2007, **111**, 14925–14931.
- 53 J. Yao, Y. Li, R. Huang, J. Jiang, S. Xiao and J. Yang, *Ionics*, 2020, **27**, 65–74.
- 54 Y. Yao, L. Zhang, Y. Gao, G. Chen, C. Wang and F. Du, *RSC Advances*, 2018, **8**, 2958–2962.
- 55 F. Gan, K. Chen, N. Li, Y. Wang, Y. Shuai and X. He, *Ionics*, 2019, **25**, 4243–4249.
- 56 J. Shi, J. Zhang and J. Guo, *ACS Energy Letters*, 2019, **4**, 2124–2129.
- 57 M. M. Rahman, M. J. Rana, S. Biswas, A. Mohammad, H. Stöcker and D. C. Meyer, *Journal of Power Sources*, 2025, **641**, 236776.

**Data availability statement**

View Article Online  
DOI: 10.1039/D5EB00054H

Due to the large volume of calculation data in this paper and the data-sharing restrictions imposed by our institution, it is not possible to upload all datasets to a public repository. However, electronic supplementary information<sup>†</sup> is provided with all the necessary information, and additional data may be made available upon request.

